Available online at www.sciencedirect.com
ScienceDirect
Nuclear Medicine and Biology 36 (2009) 551–559
NUCLEAR MEDICINE — AND — BIOLOGY
www.elsevier.com/locate/nucmedbio

Quantitative small animal PET imaging with nonconventional nuclides

Xiaodong Liu, Richard Laforest*
Mallinckrodt Institute of Radiology, Washington University School of Medicine, St. Louis, MO 63110, USA
Received 20 October 2008; received in revised form 20 December 2008; accepted 27 January 2009

Abstract

Positron Emission Tomography (PET) has gained a tremendous momentum recently for clinical applications notably with the availability of ^{18}F-fluorodeoxyglucose for staging and evaluation of therapy efficacy in various types of cancers. Nonconventional positron emitting nuclides are now being investigated for the development of novel imaging and therapeutic strategies. However, these nuclides have less than ideal imaging properties. This article compares the performance for imaging of nonconventional nuclides such as ^{61}Cu, ^{68}Ga, ^{86}Y and ^{94m}Tc with the standard imaging nuclide ^{18}F for high-resolution small animal PET imaging. Quantitative imaging performance was evaluated in terms of spatial resolution and hot spheres recovery coefficients from image resolution and image quality phantoms representing the mouse. The data were reconstructed using algorithms of 2D filtered-back-projection, 2D ordered-subsets expectation maximization and maximum-a-posteriori. It is shown that the spatial resolution point spread function can be well explained by a double-gaussian function due to the generally long range of the positron. We show that, with the knowledge of the measured point spread functions, the accurate activity concentration in small lesions can be recovered when imaging with long-range positron emitters.

Keywords: microPET; Nonconventional nuclides; Cascade γ-rays; Spatial resolution; Recovery coefficients

1. Introduction

Positron emission tomography (PET) commonly uses tracers labeled with positron emitting radioactive nuclides such as ^{11}C, ^{15}O, ^{13}N and ^{18}F. These conventional nuclides have short half-life and decay without the emission of other gamma rays which interfere with the 511-keV annihilation photons. The most widely used nuclide and imaging agent is of course ^{18}F-fluorodeoxyglucose (^{18}F-FDG) which is used clinically for staging and evaluation of cancer therapy for a wide variety of cancer types. Nonconventional radioactive nuclides such as ^{60,61,64}Cu [1–5], ^{68}Ga [6], ^{94m}Tc [7], ^{76}Br [8–11], ^{86}Y [12–15] and ^{124}I [16–18] are being investigated for novel diagnostic or internal radiotherapy strategies. The generally longer half-life of these nonconventional radioactive nuclides enables the biological processes to be studied over a longer time and allow for distribution of the nuclide to other imaging centers. However, nonconventional radioactive nuclides have usually higher positron emission energies than ^{18}F (mean value of 250 keV) and emit cascade γ-rays following the positron emission or the electron capture [19]. The longer positron range due to higher positron energies results in resolution degradation in PET. In addition, the cascade γ-rays will produce photon coincident detections that are spatially uncorrelated, resulting in the background in the emission sinograms [20–25] which will affect the quantitation accuracy. The cascade γ-rays also increase the single event rate of the PET scanner producing additional random coincidences and may lead to inaccurate dead time correction.

The aim of this work was to characterize these nuclides for quantitative PET imaging and study the effect of the loss of resolution from the positron range, especially in small animal PET imaging where most of novel imaging agent research is performed. To this end, we carefully measured the spatial resolution for a few nonconventional nuclides (^{61}Cu, ^{68}Ga, ^{94m}Tc and ^{86}Y) and the hot-sphere recovery coefficients (RCs) in a warm background. We also showed that our measurements of the point spread function with these long-range positron emitters can be used to recover the activity concentration in small volumes.

* Corresponding author. Tel.: +1 314 362 8423; fax: +1 314 362 5428.
E-mail address: laforestr@wustl.edu (R. Laforest).

0969-8051/$ – see front matter © 2009 Elsevier Inc. All rights reserved.
doi:10.1016/j.nucmedbio.2009.01.019

2. Materials and methods

Small animal PET imaging was performed using a Siemens/Concorde microPET FOCUS-F120 at the exception of the RC measurement of ^{94m}Tc which was performed in a Siemens Concorde microPET FOCUS-F220. These cameras are composed of four rings of 24 or 42 blocks of 12×12 array of (1.51×1.51×10 mm) LSO scintillation crystals [26,27]. In all cases, the phantoms were located in the center of the field of view (FOV) and images were reconstructed with a 0.4-mm pixel size by 0.796-mm slice thickness as we would do typical mice imaging in these systems. The acceptance energy window was set to 350–650 keV, and the width of coincidence timing window was 6 ns. For all studies, the injected activity in the phantoms was chosen to limit the camera deadtime below 10% or approximately 17 MBq (0.5 mCi). Data acquisition were performed for at least 30 minutes for the nonstandard nuclides and for 10 minutes for ^{18}F. The nonconventional nuclides with the exception of ^{68}Ga (obtained from TCI medical, Albuquerque, NM, USA) were produced by the cyclotron facility of Mallinckrodt Institute of Radiology [28–30]. Decay properties of these nuclides are summarized in Table 1.

For objects of this size, cascade coincidences create an approximately uniform distribution of counts for a small phantom centered in the FOV [29,32]. In this work, the scatter correction sinograms were generated from emission sinograms preprocessed by the subtraction of a uniform background component with scale factor of 0.9 at the tail edge of FOV. We used the manufacturer provided scatter correction software (3D model scatter correction). Then, the sum of cascade distribution and scatter sinogram was then used for combined scatter and cascade correction. Other methods have been applied to the correction of cascade coincidences in human scanners such as uniform background subtraction [22,24], a linear fit to the projection tails [23], modification to the scatter algorithm [7] and convolution subtraction [33]. Since our phantoms are relatively small, centered in the FOV and the cascade distributions were very uniform, the simple uniform subtraction model was used here.

Table 1
Selected nuclide decay properties

Nuclide	Half-life (h)	E_{max}/E_{avg} (MeV/MeV)	% beta Decay	Others [g (%)] (keV, %)
^{18}F	1.83	0.633/0.248	96.5	–
^{61}Cu	3.33	1.215/0.500	61.5	656 (10.8)
^{68}Ga	1.13	1.899/0.829	89.0	1077 (3.2)
^{86}Y	14.74	3.141/0.650	31.95	443 (16.9)
				628 (32.6)
				703 (15.4)
^{94m}Tc	0.87	2.439/1.072	70.0	871 (94.2)

Only the most abundant prompt gamma rays are listed. Data taken from the National Nuclear Data Center, Brookhaven National Laboratory [31].

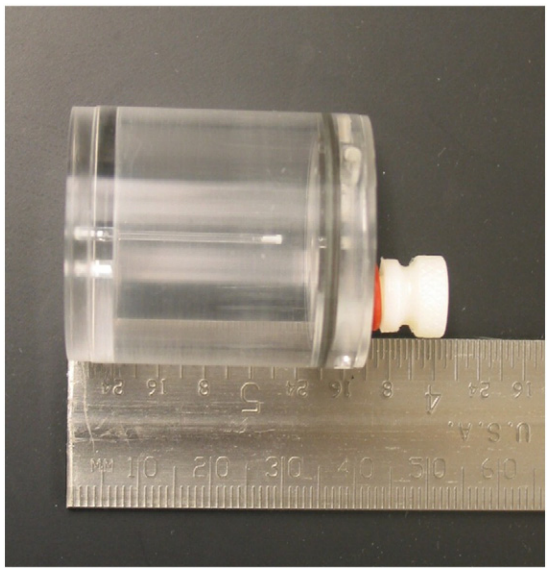

Fig. 1. The spatial resolution phantom showing the fillable 2.5-cm-diameter cylinder containing two capillary tubes inside.

2.1. Transverse spatial resolution

The spatial resolutions were measured using an imaging resolution phantom composed of a uniform cylinder in which two fillable capillary line sources were inserted. This phantom is shown in Fig. 1: the inner diameter (ID) and length of the Lucite cylinder were 25.1 mm and 26.5 mm, respectively. One capillary tube was located in the axis center of the phantom, the other one was located 8.0 mm away from the center. The outer diameter (OD) and the ID of the capillary tube were 1.0 mm and 0.25 mm, respectively. The transverse spatial resolution for each nuclide was measured in two separate scans: first, with activity in the line sources only and with the phantom filled with cold water (infinite contrast) and second, with the surrounding water containing a small amount of activity in a concentration ratio of 300:1 between line source and background area. The algorithm of 2D filtered-back-projection (2D-FBP) [with ramp filter cutoff set at 0.3, 0.35, 0.4, 0.45, 0.5 cm^{-1} (Nyquist frequency)], 2D ordered-subsets expectation maximization (2D-OSEM) (4 iterations/16 subsets) [34] and maximum a posteriori (MAP) [35,36] (20 iterations and β values of 0.5, 0.25, 0.1, 0.05 and 0.01) were used to reconstruct the images. MAP is a penalized maximum likelihood type of algorithm with system modeling of the gamma ray detection and a statistical modeling of the Poisson nature of gamma ray decay and detection. A single hyperparameter controls the importance of the regularization term (b parameter). As such, image reconstruction using a larger value of b parameter leads to smoother images, while a smaller value of b leads to crisper images with higher spatial resolution. For small values of b hyperparameter, improved spatial resolution is achieved. Image reconstruction algorithms were provided by the manufacturer. Spatial resolutions [full-width at half-

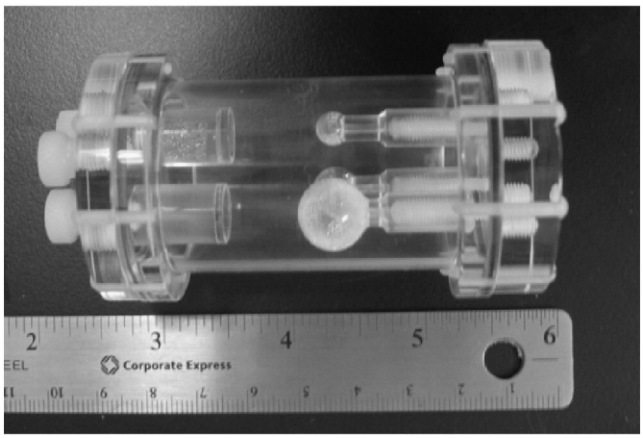

Fig. 2. Mouse size image quality phantom showing the three spheres and lung inserts. The internal dimension of the cylinder is 3 (diameter) by 5 cm (length).

maximum (FWHM)] were extracted for single plane line profiles traced through the line source image and then the average over five consecutive planes was calculated.

2.2. Hot sphere RCs

The RCs were measured by using a mouse-like image quality phantom containing three spheres (ID: 3.9, 6.2 and 9.9 mm) and two cylinders (ID: 8 mm, OD: 10 mm) as shown in Fig. 2. The ID and length of this water-fillable cylinder phantom is 3.0 cm and 5.0 cm, respectively. The phantom was prepared with an activity concentration ratio of 10.1:1 between the hot spheres and the uniform area for all nuclides. The two small cylinders did not contain activity: one was left empty with air and the other one contained cold water.

Images were reconstructed with the image reconstruction algorithms mentioned above with cascade, scatter, attenuation, deadtime corrections and normalization. The mean values of the warm background were measured in the uniform region inside the phantom. The mean values of the spheres were measured in regions of interest (ROI), with the boundary set at 20–90% of the maximum value in the specific sphere in the plane containing the largest section of the sphere. The RC is defined by the ratio of mean value in ROI to the known activity value in the sphere. The scanner was calibrated for each nuclide by ensuring the activity in the uniform area in the phantom matched the expected activity.

Due to image blurring caused by the limited spatial resolution and, in particular, due to the long positron range, the measured activity in small volume is smaller than expected in small animal PET. The measured activity in the spheres can thus generally be expressed as:

$$M_{\text{sphere}} = A_{\text{sphere}} R_{\text{sphere}} + A_{\text{uniform}} S_{\text{uniform}\rightarrow\text{sphere}} \quad (1)$$

where A_{sphere} and A_{uniform} are the known activity concentrations in the sphere and in the uniform area; R_{sphere} and $S_{\text{uniform}\rightarrow\text{sphere}}$ are the recovery fraction from the sphere and the spill-over fraction from the uniform area into the sphere. The values of R_{sphere} and $S_{\text{uniform}\rightarrow\text{sphere}}$ can be calculated by a 3D convolution of the measured point spread function with a numerical mock of the image quality phantom knowing the exact dimensions of the phantom, including the spheres.

3. Results

3.1. Line spread function and point spread function

Fig. 3A and B shows the line source image profiles for ^{18}F and ^{94m}Tc in cold water reconstructed by 2D-FBP

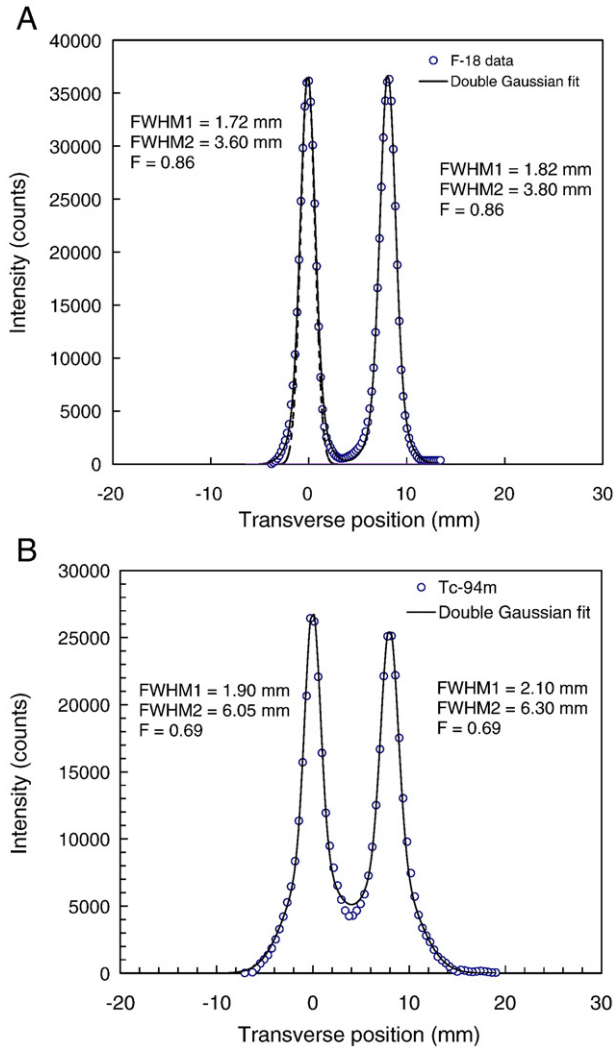

Fig. 3. (A and B) Image profile traced through the two line source filled with ^{18}F (A) and ^{94m}Tc (B) surrounded by nonradioactive water. Each peak of the profile is fitted by double Gaussian function with the fit parameters displayed on the graph.

algorithm. It can be well characterized by a double Gaussian function:

$$F(x) = F\exp\left(\frac{-x^2}{2\sigma_1^2}\right) + (1-F)\exp\left(\frac{-x^2}{2\sigma_2^2}\right) \quad (2)$$

For the capillary line source at the center of the FOV, the FWHM of first Gaussian function is 1.90 mm, and the second Gaussian function is 6.05 mm for ^{94m}Tc. Clearly, a simple Gaussian distribution cannot explain the measured distribution as is usually done in spatial resolution measurements. For the line source located at 8 mm radial offset, the FWHMs were slightly larger than the center one, reflecting the fact that the spatial resolution is somewhat better at the center of the tomograph. The point spread function (PSF) can be converted from the line spread function (LSF) by:

$$g(x) = \frac{W}{\left(\sqrt{2\pi}\sigma_1\right)^3}\exp\left(-\frac{x^2}{2\sigma_1^2}\right) + \frac{1-W}{\left(\sqrt{2\pi}\sigma_2\right)^3}\exp\left(-\frac{x^2}{2\sigma_2^2}\right) \quad (3)$$

where

$$W = \frac{F\sigma_1^2}{F\sigma_1^2 + (1-F)\sigma_2^2} \quad (4)$$

The distribution for ^{18}F and ^{94m}Tc are shown here. The other radionuclides considered in this work exhibit similar double gaussian distribution with different fitting parameters. Fig. 4 presents the correlation between the root mean square radius of the PSF (constructed by FBP with Ramp filter cutoff at 0.5 cm^{-1}) to the mean energy of positron. Table 2 compiles the fit parameters (by nonlinear least square minimization) for all other nuclides and for the different image reconstruction algorithms. We can note that even for ^{18}F, a double gaussian fit predicts a better description of the observed line profile. The F factor is large, however, indicating that the positron range has a small contribution to the loss of resolution.

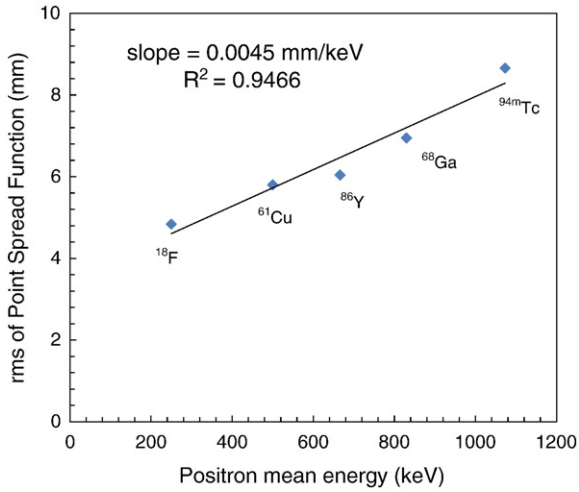

Fig. 4. Root mean square of 2D-FBP point spread function plotted as a function of the average positron energy from each nuclide.

Table 2
Double-gaussian-fit parameters and weights of the LSF and point spread function for the nuclides considered in this work

Algorithms	Nuclides	FWHM$_1$ (mm)	FWHM$_2$ (mm)	F	W
2D-FBP	^{18}F	1.82	4.00	0.89	0.63
	^{61}Cu	1.93	4.20	0.74	0.37
	^{68}Ga	2.19	5.40	0.59	0.19
	^{94m}Tc	1.99	5.42	0.61	0.17
	^{86}Y	1.86	4.05	0.63	0.26
2D-OSEM	^{18}F	0.98	2.78	0.77	0.29
	^{61}Cu	1.68	3.33	0.70	0.37
	^{68}Ga	1.4	3.91	0.62	0.17
	^{94m}Tc	1.74	6.00	0.73	0.19
	^{86}Y	0.86	3.4.0	0.57	0.08
MAP (b=0.01)	^{18}F	1.06	2.95	0.94	0.67
	^{61}Cu	1.18	3.30	0.96	0.75
	^{68}Ga	1.32	4.20	0.88	0.42
	^{94m}Tc	1.42	5.80	0.85	0.25
	^{86}Y	1.16	3.20	0.80	0.34

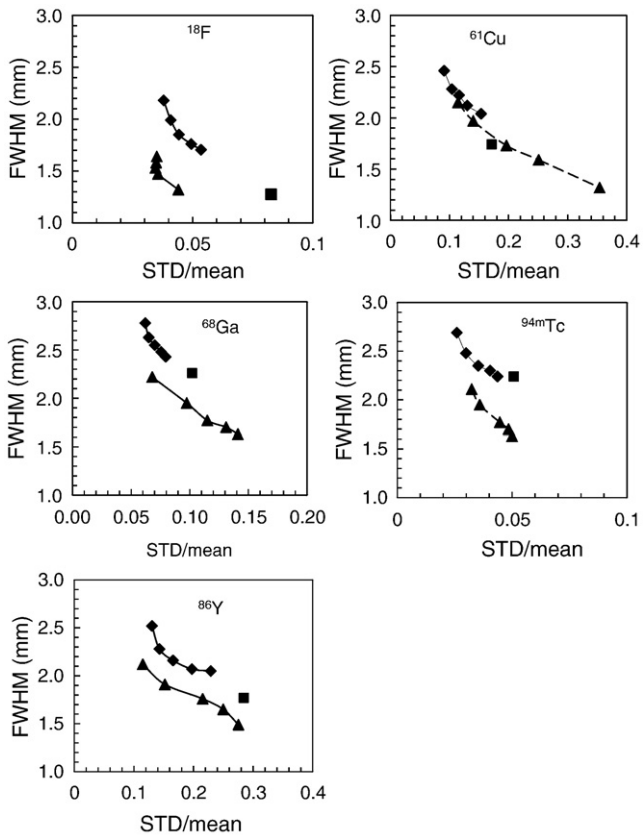

Fig. 5. Spatial resolution plots versus noise (defined as the standard deviation in the uniform area) for ^{18}F, ^{61}Cu, ^{68}Ga, ^{94m}Tc and ^{86}Y for 2D-FBP (diamonds), 2D-OSEM (squares) and MAP (triangles).

3.2. Spatial resolution vs. noise

The relative image noise was extracted by the ratio of standard deviation over mean value (S.D./mean) of an ROI traced in the uniform area of the phantom from the scans filled in the 300:1 ratio. The spatial resolutions were measured for the capillary line source at the center of the FOV. The relations of spatial resolution as a function of image noise are presented in Fig. 5 for the different nuclides.

2D-FBP (diamonds) gave best resolution and largest noise when the ramp filter cutoff value is 0.5 cm^{-1} (Nyquist frequency). At this cutoff frequency, the measured FWHMs were 1.73, 2.04, 2.43, 2.24 and 2.05 mm for ^{18}F, ^{61}Cu, ^{68}Ga, ^{94m}Tc and ^{86}Y, respectively. The 2D-OSEM normally gave better resolution than 2D-FBP. The spatial resolution FWHM by 2D-OSEM were 1.51, 1.74, 2.26, 2.01 and 1.77 mm for ^{18}F, ^{61}Cu, ^{68}Ga, ^{94m}Tc and ^{86}Y, respectively. The spatial resolutions by 3D-MAP algorithm were even better than 2D-OSEM when b value in 3D-MAP was set to 0.01. At this value of b parameter, the spatial resolution FWHM by MAP were 1.32, 1.32, 1.53, 1.63 and 1.49 mm for ^{18}F, ^{61}Cu, ^{68}Ga, ^{94m}Tc and ^{86}Y, respectively. For all nuclides, we note that MAP produces better spatial resolution at essentially all values of b parameter and that the noise level is lower for most nuclides.

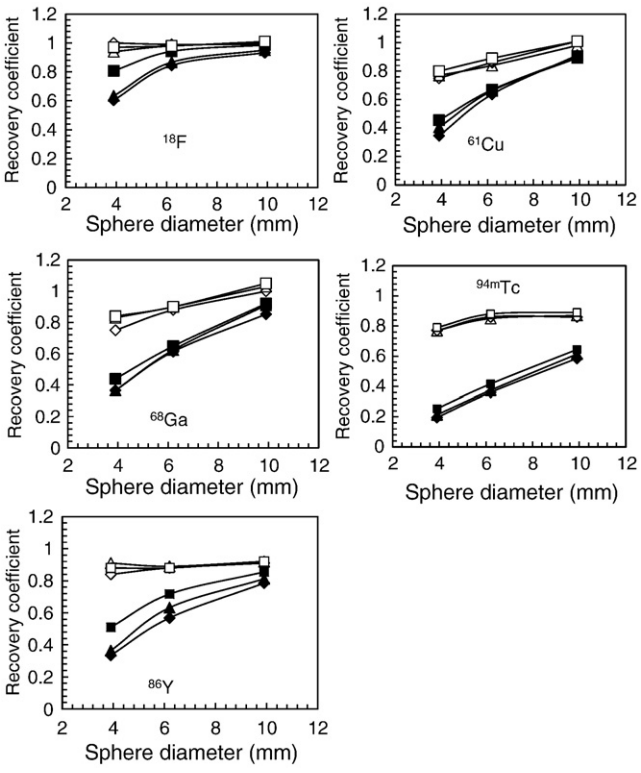

Fig. 6. RCs for ^{18}F, ^{61}Cu, ^{68}Ga, ^{94m}Tc and ^{86}Y for the different sphere diameters for the boundary threshold of the ROI was 80%. Open symbols were corrected for partial volume using the measured point spread function for each nuclide: 2D-FBP (diamonds), 2D-OSEM (squares) and MAP (triangles).

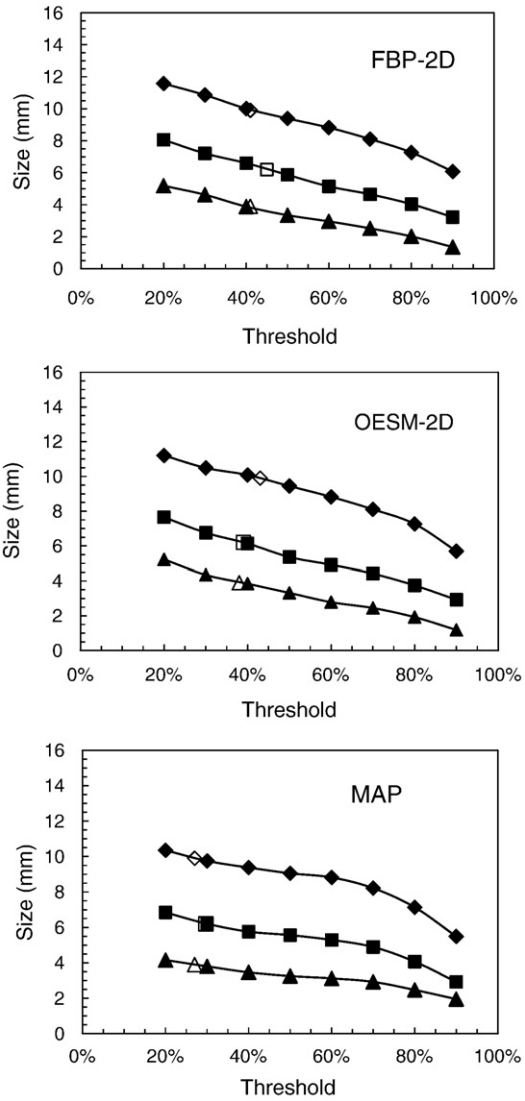

Fig. 7. Apparent sphere size plotted for the different ROI thresholds for ^{18}F by 2D-FBP (diamonds), 2D-OSEM (squares) and MAP (triangles) algorithm. The open symbols indicate the critical thresholds leading to the actual sphere sizes.

3.3. Hot sphere RCs

RCs were extracted for different volume of spheres and different boundary thresholds of ROI. Fig. 6 shows the measured RCs for the three spheres. The threshold of ROI was set here at 80% of the maximum intensity in the given sphere. The ramp cutoff parameter for 2D-FBP was set to 0.5cm^{-1}. The b value of MAP algorithm was set to 0.01 and reconstructions were performed for 20 iterations. The solid symbols represent the RCs before partial volume correction. The values of RC in smaller spheres are less than the values in larger spheres. The open symbols are the

RC after partial volume correction. The corrected RCs for ^{18}F are close to 100%.

Since other nuclides have longer positron range than ^{18}F, the RCs before partial volume correction were lower. After partial volume correction, the RCs for ^{61}Cu and ^{68}Ga for the large sphere were close to 100%; the RCs in medium and smallest spheres ranged from 75% to 90%. These results illustrate that the measured PSF are accurate characterization of the system resolution for these nuclides.

The nuclides ^{94m}Tc and ^{86}Y have even lower values of RC than ^{61}Cu and ^{68}Ga before partial volume correction. After correction, the RC of ^{94m}Tc ranged 85% to 89% for large and medium spheres and close to 78% for the small sphere; the RC of ^{86}Y ranged 88% to 92% for large and medium spheres and varied from 84% to 91% for the small sphere. These results illustrate that the partial volume correction for ^{94m}Tc and ^{86}Y almost completely compensates for the reduced RCs.

3.4. Apparent sphere size and ROI threshold level

Fig. 7 shows the diameters of ROI as a function of ROI threshold value for ^{18}F. The open symbols represent the critical threshold corresponding to the true sphere sizes. For 2D-FBP, the critical thresholds are 41%, 45% and 41% for large, medium and small spheres, respectively. For 2D-OSEM, the critical thresholds are 43%, 39% and 38%, respectively. For MAP, the thresholds are 27%, 30% and 27%, respectively.

Fig. 8 shows the critical thresholds corresponding to the true sphere size for all the nuclides. The critical thresholds of nonstandard nuclides are higher than those of ^{18}F. It can be

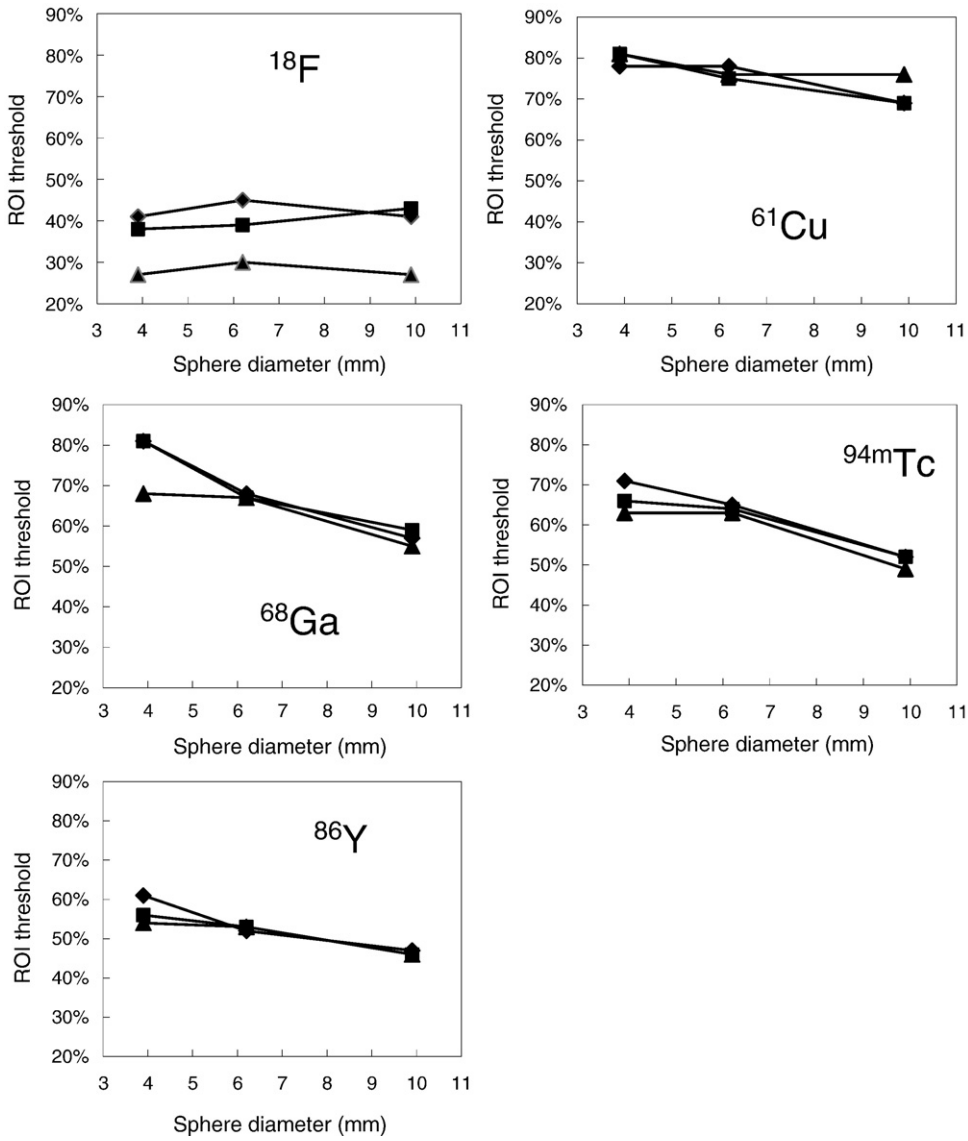

Fig. 8. Critical ROI thresholds yielding the actual sphere size for the different nuclides indicated: 2D-FBP (diamonds), 2D-OSEM (squares), MAP (triangles).

seen that the critical thresholds of ^{18}F show a dependence on the reconstruction algorithms, while the nonstandard nuclides are almost independent on the choice of image reconstruction algorithm.

4. Discussion

The positron range clearly degrades the spatial resolution in high-resolution small animal PET imaging. Higher positron energy results in longer positron range and wider profiles of LSF and PSF. The profiles of LSF and PSF could be well characterized by double Gaussian functions a narrower gaussian distribution dominates the spatial resolution component due to the intrinsic scanner resolution and reconstruction algorithm and a second wider gaussian distribution due to the extended positron range. Both effects contribute to reducing the contrast and thus the RCs in small objects.

For each nuclide, the resolution achieved by 2D-OSEM is better than the 2D-FBP at the center of the FOV; while the best resolution from MAP is even better than that from OSEM. The correlation of image noise and spatial resolution indicates that at a given spatial resolution, MAP reconstruction generally yields to less noisy images. The noise level in the images will obviously depends on the reconstruction resolution and statistics. For all the studied nuclides, the 2D-OSEM algorithm gives higher noise than 2D-FBP.

The RC for ^{18}F with the smallest sphere was mainly caused by the loss of resolution due to intrinsic scanner resolution since the positron range is relatively small for this nuclide. The spheres' activity concentration could be recovered very accurately using the measured PSF thus validating the measurements. Even without partial volume correction, the 3D-MAP algorithm normally gives higher RCs than the other algorithms since this algorithm recovers partially for the loss of spatial resolution caused by the finite detector size and annihilation photon acolinearity. For nonconventional nuclides, the positron range is longer than ^{18}F and is the dominant factor affecting spatial resolution. Accurate activity concentration can be achieved by employing partial volume corrections using a nuclide specific PSF. We have seen that our measurements of the PSF for the different nonstandard nuclides considered here can compensate almost completely for the loss of RC.

Interestingly, the choice of nuclides in this work provides for a constant gradation of the average positron range energy, ranging to the smallest available with ^{18}F to ^{94m}Tc, and this is reflected in the measured root mean square of the PSF presented in Fig. 4. As expected, the uncorrected RCs are also smaller for the larger root mean square resolution values. Spatial resolution can be decomposed into several components: intrinsic from detector size, annihilation photon non-acolinearity, cross-talk in a block detector, depth of interaction effect and positron range [19,37]. Apart from the depth of interaction, all other parameters are spatially invariant. Thus, if the spatial resolution is known at all positions in the FOV for a very short range positron emitter as measured for ^{22}Na in Refs. [26,27], the nuclide specific and spatially variant point spread function can be deduced.

When anatomical images are not available, tumor size measurement may only be done using the PET images, and due to limitation in spatial resolution, tumor size enclosed by ROI will depend on the ROI threshold. For cervical cancer using ^{18}F-FDG PET, Miller and Grigsby [38] found a good correlation at 40% threshold value with tumor size extracted from X-ray computed tomography. A further evaluation of lesion size extraction from clinical PET data is presented in [39]. The critical threshold to give the true volume (or diameter) of the spheres (tumors) depends on the PSF of each tracer, which is determined by the positron emission range and reconstruction algorithm. Since the nonconventional nuclides have long positron range, they have larger value of critical thresholds. Our data also indicate that those thresholds are approximately independent of tumor size.

This article shows that nuclide specific accurate characterization of system performance is crucial for quantitative small animal PET imaging with nonstandard nuclides, whether a simple partial volume correction is used or a more complex technique such as in an image restoration by an iterative deconvolution process [40] or in iterative image reconstruction aiming at the recovery for the loss of resolution due to the positron range [5,35].

5. Conclusion

Due to the longer positron range and cascade gamma decay, the nonconventional nuclides normally cause degraded spatial resolution and consequently lower RCs than short-range positron emitting nuclides such as ^{18}F. The spatial resolutions of ^{61}Cu, ^{68}Ga, ^{94m}Tc and ^{86}Y have been extracted from line source phantom and compared to ^{18}F. The LSFs and PSFs were characterized by double Gaussian functions. The RCs of the above nuclides have been extracted for spheres of different diameters in an image quality phantom. Our results show that the loss of RC is caused by the loss of resolution due to the positron range. The accurate characterization of the PSF allowed for compensation of the loss in RC using calculated spill-over and partial volume corrections. The dependence of apparent sphere size as a function of ROI threshold was analyzed. These data are helpful when one needs to extract lesion size from PET images.

Acknowledgments

This work was supported by a grant from the NIH-NCI, the Radionuclide Resource for Cancer Applications (RRCA 1 R24 CA86307). The authors thank Lucie Tang, P.Eng., for

help in phantom design and construction. We are also grateful to the RRCA team and the cyclotron facility staff of Washington University School of Medicine for production of the radionuclides.

References

[1] Williams H, Robinson S, Julyan P, Zweit J, Hastings D. A comparison of PET imaging characteristics of various copper radioisotopes. Eur J Nucl Med Mol Imag 2005;32(12):1473–80.
[2] Smith SV. Molecular imaging with copper-64. J Inor Biochem 2004;98 (11):1874–901.
[3] Lewis JS, Laforest R, Buettner TL, Song SK, Fujibayashi Y, Connet JM, et al. Copper-64-diacetyl-bis(*N*4-methylthiosemicarbazone): an agent for radiotherapy. Proc Nucl Acad Scie 2001;98(3):1206–11.
[4] Dehdashti F, Grigsby PW, Lewis JS, Laforest R, Siegel BA, Welch MJ. Assessing tumor hypoxia in cervical cancer by PET with 60Cu-labeled diacetyl-bis(*N*4-methylthiosemicarbazone). J Nucl Med 2008;49(2): 201–5.
[5] Ruangma A, Bai B, Lewis JS, Sun X, Welch MJ, Leahy RM, et al. Three-dimensional maximum a posteriori (MAP) imaging with radiopharmaceuticals labeled with three Cu radionuclides. Nucl Med Biol 2006;33:217–26.
[6] Smith-Jones PM, Stolz B, Bruns C, Albert R, Reist H, Fridrich R, et al. Gallium-67/gallium-68-[DFO]-octreotide — a potential radiopharmaceutical for PET imaging of somatostatin receptor-positive tumors: synthesis and radiolabeling in vitro and preliminary in vivo studies. J Nucl Med 1994;35(2):317–25.
[7] Barker WC, Szajek LP, Green SL, Carson RE. Improved quantification for Tc-94m PET imaging. IEEE Trans Nucl Sci 2001;48(3):739–42.
[8] Dupont S, Semah F, Loc'h C, Strijckmans V, Baulac M, Samson Y, et al. In vivo imaging of muscarinic cholinergic receptors in temporal lobe epilepsy with a new PET tracer: [76Br]4-bromodexetimide. J Nucl Med 1999;40(6):935–41.
[9] Lovqvist A, Lundqvist H, Lubberink M, Tolmachev V, Carlsson J, Sundin A. Kinetics of [sup 76]Br-labeled anti-CEA antibodies in pigs; aspects of dosimetry and PET imaging properties. Med Phys 1999;26(2):249–58.
[10] Ribeiro MJ, Almeida P, Strul D, Ferreira N, Loc'h C, Brulon Vt, et al. Comparison of fluorine-18 and bromine-76 imaging in positron emission tomography. Eur J Nucl Med Mol Imag 1999;26 (7):758–66.
[11] Lubberink M, Schneider H, Bergstromm M, Lundqvist H. Quantitative imaging and correction for cascade gamma radiation of ^{76}Br with 2D and 3D PET. Phys Med Biol 2002;47(19):3519.
[12] Lovqvist A, Humm JL, Sheikh A, Finn RD, Koziorowski J, Ruan S, et al. PET imaging of 86Y-labeled anti-Lewis Y monoclonal antibodies in a nude mouse model: comparison between 86Y and 111In radiolabels. J Nucl Med 2001;42(8):1281–7.
[13] Herzog H, Rosch F, Stocklin G, Lueders C, Qaim SM, Feinendegen LE. Measurement of pharmacokinetics of yttrium-86 radiopharmaceuticals with PET and radiation dose calculation of analogous yttrium-90 radiotherapeutics. J Nucl Med 1993;34(12):2222–6.
[14] Walrand S, Jamar F, Mathieu I, De Camps J, Lonneux M, Sibomana M, et al. Quantitation in PET using isotopes emitting prompt single gammas: application to yttrium-86. Eur J Nucl Med Mol Imag 2003; 30(3):354–61.
[15] Pagani M, Stone-Elander S, Larsson SA. Alternative positron emission tomography with non-conventional positron emitters: effects of their physical properties on image quality and potential clinical applications. Eur J Nucl Med Mol Imaging 1997;24(10):1301–27.
[16] Pentlow KS, Graham MC, Lambrecht RM, Cheung NKV, Larson SM. Quantitative imaging of I-124 using positron emission tomography with applications to radioimmunodiagnosis and radioimmunotherapy. Med Phys 1991;18(3):357–66.
[17] Flower MA, Al-Saadi A, Harmer CL, McCready VR, Ott RJ. Dose-response study on thyrotoxic patients undergoing positron emission tomography and radioiodine therapy. Eur J Nucl Med Mol Imaging 1994;21(6):531–6.
[18] Gonzalez Trotter DE, Manjeshwar RM, Doss M, Shaller C, Robinson MK, Tandon R, et al. Quantitation of small-animal 124I activity distributions using a clinical PET/CT scanner. J Nucl Med 2004;45(7): 1237–44.
[19] Laforest R, Rowland DJ, Welch MJ. MicroPET imaging with nonconventional isotopes. IEEE Trans Nucl Sci 2002;49(5): 2119–26.
[20] Schueller MJ, Mulnix TL, Christian BT, Jensen M, Holm S, Oakes TR, et al. Addressing the third gamma problem in PET. IEEE Trans Nucl Sc 2003;50(1):50–2.
[21] Martin CC, Christian BT, Satter MR, Nickerson LDH, Nickles RJ. Quantitative PET with positron emitters that emit prompt gamma rays. IEEE Trans Med Imaging 1995;14(4):681–7.
[22] Pentlow KS, Finn RD, Larson SM, Erdi YE, Beattie BJ, Humm JL. Quantitative imaging of yttrium-86 with PET: the occurrence and correction of anomalous apparent activity in high density regions. Clin Pos Ima 2000;3:85–90.
[23] Kohlmyer SG, Miyaoka RS, Shoner SC, Lewellen TK, Eary JF. Quantitative accuracy of PET imaging with yttrium-86. J Nucl Med 1999;40(5):280P.
[24] Lubberink M, et al. Correction for gamma radiation from non-pure positron emitters in positron emission tomography. Future Directions in Nuclear Medicine Physics and Engineering. Chicago: The University of Chicago; 1999.
[25] Herzog H, Tellmann L, Qaim SM, Spellerberg S, Schmid A, Coenen HH. PET quantitation and imaging of the non-pure positron emitting iodine isotope I-124. Appl Radiat Isot 2002;56(5):673–9.
[26] Laforest R, Longford D, Siegel S, Newport DF, Yap J. Performance evaluation of the microPET (R)-FOCUS-F120. IEEE Trans Nucl Sci 2007;54(1):42–9.
[27] Tai YC, Ruangma A, Rowland D, Siegel S, Newport D, Chow P, et al. Performance evaluation of microPET focus: a third generation microPET Scanner dedicated to animal imaging. J Nucl Med 2005; 45:455–63.
[28] McCarthy DW, Bass LA, Cutler PD, Shefer RE, Klinkowstein RE, Herrerro P, et al. High purity production and potential applications of copper-60 and copper-61. Nucl Med Biol 1999;26:351–8.
[29] Biggot H, Laforest R, Liu X, Ruangma A, Wuest F, Welch MJ. Advances in the production, processing and microPET image quality of technetium-94m. Nucl Med Biol 2006;33:923–33.
[30] Yoo J, Tang L, Perkins TA, Rowland DJ, Laforest R, Lewis JS, et al. Preparation of high specific activity (86)Y using a small biomedical cyclotron. Nucl Med Biol 2005;32(8):891–7.
[31] NNDC (National Nuclear Data Center). Medical internal radiation dosimetry. http://www.nndc.bnl.gov/mird/.
[32] Laforest R, Liu X. Image quality with non-standard nuclides in PET. Q J Nucl Med Mol Imaging 2008;52:151–8.
[33] Beattie BJ, Pentlow KS, Finn RD, Larson SM. A method for the removal of spurious activity in PET imaging introduced by cascade gamma rays. J Nucl Med 2001;42(5):201P.
[34] Hudson HM, Larkin LS. Accelerated image reconstruction using ordered subsets of projection data. IEEE Trans Med Imaging 1994; 13(4):601–9.
[35] Qi J, Leahy RM, Cherry SR, Chatziioannou A, Farquhar TH. High-resolution 3D Bayesian image reconstruction using the microPET small-animal scanner. Phys Med Biol 1998;43:1001–13.
[36] Chatziioannou A, Qi J, Moore A, Annala A, Nhuyen K, Leahy R, et al. Comparison of 3-D maximum a posteriori and filtered backprojection algorithms for high-resolution animal imaging with microPET. IEEE Trans Med Imaging 2000;19(5):507–12.
[37] Levin CS, Hoffman EJ. Calculation of positron range and its effect on the fundamental limit of positron emission tomography system spatial resolution. Phys Med Biol 1999;44:781.

[38] Miller TR, Grigsby PW. Measurement of tumor volume by PET to evaluate prognosis in patients with advanced cervical cancer treated by radiation therapy. Int J Radiat Oncol Biol Phys 2002;53(2):353–9.

[39] Ford EC, Kinahan PE, Hanlon L, Alessio A, Rajendran J, Schwartz DL, et al. Tumor delineation using PET in head and neck cancers: threshold contouring and lesion volumes. Med Phys 2006;33(11): 4280–8.

[40] El Naqa I, Low DA, Bradley JD, Vicic M, Deasy JO. Deblurring of breathing motion artifacts in thoracic PET images by deconvolution methods. Med Phys 2006;33(10):3587–600.